Digital imaging scanning system and biomedical applications for biochips

Guoliang Huang
Cheng Deng
Jiang Zhu
Shukuan Xu
Chao Han
Tsinghua University
School of Medicine
Medical Systems Biology Research Center
100084, Beijing, China
    and
National Engineering Research Center
    for Beijing Biochip Technology
102206, Beijing, China
E-mail: tshgl@tsinghua.edu.cn

Xiaobo Song
Xiaoyong Yang
National Engineering Research Center
    for Beijing Biochip Technology
102206, Beijing, China

Abstract. Biochips have been an advanced technology for biomedical applications since the end of the 20th century. Optical detection systems have been a very important tool in biochip analysis. Microscopes are often inadequate for high resolution and big view-area detection of microarray chips, thus some new optical instruments are required. In this work, a novel digital imaging scanning system with dark-field irradiation is developed for some biomedical applications for microarray chips, characterized by analyzing genes and proteins of clinical samples with high specific, parallel, and nanoliter samples. The novel optical system has a high numerical aperture (NA=0.72), a long working distance ($w_d > 3.0$ mm), an excellent contrast and signal-to-noise ratio, a high resolving power close to 3 μm, and an efficiency of collected fluorescence more than two-fold better than that of other commercial confocal biochip scanners. An edge overlap algorithm is proposed for the image restructure of free area detection and correcting scanning position errors to a precision of 1 pixel. A novel algorithm is explored for recognizing the target from the scanning images conveniently, removing noise, and producing the signal matrix of biochip analysis. The digital imaging scanning system is equally as good for the detection of enclosed biochips as it is for the detection of biological samples on a slide surface covered with a glass cover slip or in culture solution. The clinical bacteria identification and serum antibody detection of biochips are described. © *2008 Society of Photo-Optical Instrumentation Engineers.* [DOI: 10.1117/1.2939402]

Keywords: microscope; biochip; microarray chip; digital imaging scanning system.

1 Introduction

Biochips were first reported by Fodor et al. in 1991.[1] They represent an advanced method for molecular detection of genes and proteins on solid surfaces, and are used for biomedical research and diagnostics. Biochip technology has advanced tremendously in recent years, and many new systems have been developed for different purposes. Examples include the microarray chip (gene and protein chips), the cell chip, and the tissue chip.[2–6] For many of these small biochips, typical applications have been for the semiquantitative detection of DNA by hybridization, quantitation of proteins by immuno-reactions, drug discovery, and drug development.[7–9] A number of important different biochip detection systems,[1–13] including fluorescence microscope imaging systems and laser confocal scanners, have been built to detect the different signals produced on the biochip surface. Signal detection requires a variety of different imaging devices, as some applications such as very high density chips require very high resolving power, while others are less demanding. In many systems, digital fluorescent imaging is used to test the entire probe surface of the biochip in a single imaging process without scanning. A costly cooled charge-coupled device (CCD) is used to obtain the fluorescent images; however, the imaging area is limited by high resolving power required for high density chips. For example, if a 1024×1024 cooled CCD detector is used in a fluorescence imaging system, a 5×5-mm object can be imaged with a resolving power of 5 μm. However, if the object is enlarged to 20×20 mm, then the imaging resolving power is reduced significantly, to only 20 μm. Typically the larger the imaging area, the lower image resolving power is available from the system. The Gene-Chip Scanner 3000 with CCD imaging developed by the Affymetrix Corporation (USA) is a digital imaging and scanning system built to accommodate special Affymetrix genechips. These chips are produced through a unique photolithographic manufacturing process and have a large number of exact fixed-position edge mark zones on the chip, required for imaging small regions. Because of the absence of gene probes on these fixed-position edge mark zones, all images produced from these small imaging regions can be simply patched, based on the fixed-position edge mark. However, for general biochips produced by standard microarray printing processes,

Address all correspondence to Guoliang Huang, The School of Medicine, Tsinghua University, Beijing, Haidian, Tsinghua Road 1-Beijing, Beijing 100084 China; Tel: 86–10–62772239; Fax: 86–10–80726769; E-mail: tshgl@tsinghua.edu.cn

it is not convenient to print the exact-fixed position edge mark zones, hence different patching approaches and image reconstructions tools are required for imaging the large surface of the chip. Expensive instruments—confocal laser scanners—are typically used for general biochip scanning applications to detect fluorescent signals. Although a photo multiplier tube (PMT) is used to obtain high precision images, the scanning resolving power is limited by the precision of motion of the moving stage required to load biochips. One popular confocal laser scanner, such as the ScannerArray 4000B, has at best a resolving power of only 5 μm. The GenePix 4000B Scanner (Molecular Devices Corporation, USA) is not a true confocal scanner because, although it employs the same scanning method as a confocal scanner, it detects fluorescent signals from the biochip by a PMT, not by CCD digital imaging. In all biochip detection systems, optical design plays a key role in obtaining a clear image of the biochip, and the optical objective is crucial to the sensitivity, resolving power, and working distance of the biochip detection system.

New detection systems capable of high sensitivity and high resolving power, with simple lens set structures and relatively low cost, are required. An objective with a high numerical aperture would provide such a solution, as it not only has excellent resolving power, but also has high efficiency for collection of fluorescent signals, allowing for highly sensitive detection of different biological molecules on the biochip surface. In this work, a novel optical imaging structure design and a digital imaging scanning system with high resolving power free-area detection is described. It employs a developed objective with a long working distance (w_d=3.0 mm) and high numerical aperture (NA=0.72). Also, the system employs an edge overlap algorithm for correcting scanning position errors in the process of restructuring of large 20 ×60-mm combined images. An analyzing algorithm is also employed to discriminate the gene (or protein) target, to remove the noise of the image, and to produce the signal matrix for analysis of the biochip. This work includes descriptions of its use in two different clinical applications.

2 Developed Digital Imaging Scanning System

2.1 New Optical Imaging System Design

The design of a digital imaging optical system with high performance detection of biological sample slides and biochips centers around the image quality, including the consideration of the resolution, zoom, aberration, and optical transfer functions, each of which can be optimized by using rays tracing calculations. All parameters of optical system structure, including the surface curvature radius of every lens, the thickness, the material used, the separation distance, and the surface aperture, were varied to obtain an excellent optical specificity and image quality, including high resolving power, appropriate zoom, low aberration, and high optical transfer functions. The functional relationships between the specificity, image quality, and structural parameters of the system can be described as follows:
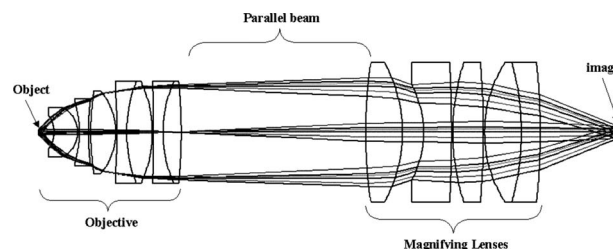
Fig. 1 Optical structure design of the digital imaging optical system.

$$\begin{cases} \aleph_1(\chi_1, \cdots, \chi_i) = \Phi_1 \\ \quad \cdots \\ \quad\quad \cdots \\ \quad \cdots \\ \aleph_k(\chi_1, \cdots, \chi_i) = \Phi_k \end{cases}, \qquad (1)$$

where i and k are two natural numbers, $\Phi_1 \ldots \Phi_k$ denote various aberrations of the optical specificity and the image quality, $\aleph_1 \ldots \aleph_k$ are functions of the specificity, the image quality, and the structural parameters of system, and $\chi_1 \ldots \chi_i$ correspond to all the structural parameters of system. Based on the polynomial expansion and the minimum binary iterative method, when all structural parameters $\chi_1 \ldots \chi_i$ are modified repeatedly, an approximate minimum aberration can be obtained using Eq. (1). To reduce material difference errors in optical machining, we design optical structures with only three glass materials. This is a minimum glass materials structure when compared with Zeiss and Nikon high numerical aperture objective products, in which five glass materials are used.

Based on this optical design method, an optimum digital imaging optical system structure for the detection of biochips is shown in Fig. 1 and the contents listed in Table 1. The optical imaging system is composed of a set of objective and magnifying lenses. The objective set is a combination of seven lenses including two doublets, and uses only three glass materials, ZF2, ZK7, and ZK11. The objective has a high numerical aperture of 0.72 for collecting the signal from the object, a focal length of 13.06 mm, and a front focal length of 3.22 mm to provide a working distance of approximately 3 mm. There is a parallel ray path between the objective and the magnifying lenses, to which it is convenient to also add filters and other optical elements. The magnifying lenses consist of five lenses with one set of doublets. This optical system has a zoom of 2.26. Because of its high numerical aperture and long working distance, our developed optical imaging scanning system is convenient for use with biochips with paling height of about 0.8 to 2.0 mm. This long working distance provides space for materials on the chip surface, such as for the positioning of cells and tissue samples, even space for a thin layer of culture solution or a glass cover slip. In comparison, general microscopes with an objective with has a numerical aperture of 0.65 have a working distance of <1 mm. This distance is not sufficient to accommodate high paling biochips, or cells and tissue samples under a culture solution or a cover slip.

Table 1 Optimization of the digital imaging scanning system (units: mm).

Surface	Radius	Thickness	Glass
1	−6.088	5.16	ZK11
2	−5.764	0.30	
3	−25.000	2.01	ZF2
4	50.350	0.54	
5	67.840	5.38	ZK7
6	−13.817	0.30	
7	−106.500	2.08	ZF2
8	29.990	5.58	ZK7
9	−25.590	0.30	
10	−306.540	2.00	ZF2
11	26.360	4.02	ZK7
12	−98.860	100.00	
13	97.520	8.00	ZK7
14	−31.008	4.60	
15	−21.760	6.07	ZF2
16	−267.900	0.31	
17	49.430	6.56	ZK7
18	−215.300	0.30	
19	27.670	8.00	ZK7
20	−55.130	4.04	ZF2
21	−160.920		

2.2 Analysis of the New Digital Imaging Optical System Design

In a fluorescence imaging system, the objective collected the emission fluorescence (em-fluor) bound on the biochip, as shown in Fig. 2, which is ideally a spherical wave,
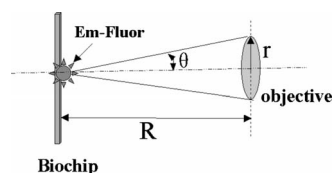
Fig. 2 Configuration of the objective collecting fluorescence.

$$\zeta(R) = \frac{K_0}{R} \times \exp[i(\omega t - kR)], \qquad (2)$$

where K_0 is a constant, ω is the angle frequency, k is the wave number, R is the radius from the center of source, and t is time.

The intensity of emission fluorescence is,

$$I(R) = \int \int \zeta(x,y,R) \times \zeta^*(x,y,R) \times dxdy \approx \frac{K_0^2}{R^2} \times \pi \times r^2, \qquad (3)$$

where K_0 is a constant, R is the distance from the center of source to the first surface of the objective, and r is the radius of effective aperture of the objective.

When a biochip is placed at the focal plane of the objective, and the objective has a numerical aperture $NA = n \times \sin \theta$, $tg\,\theta = r/R$, where n is the refractive index, then Eq. (3) can be simplified as Eq. (4):

$$I(R) \approx \frac{1}{n^2} \times K_0^2 \times \pi \times NA^2 \times (1 + NA^2 + NA^4 + \dots). \qquad (4)$$

Equation (4) indicates that the intensity of the collected emission fluorescence on the biochip has a direct ratio to the square of NA and other higher powers of NA. By analyzing Eq. (4), we see that our high numerical aperture (NA=0.72) objective digital imaging scanning system has an efficiency of collected emission fluorescence more than two-fold. This is significantly better than that of other commercial confocal biochip scanners,[8,9] which have objectives with smaller numerical apertures than 0.5.

The optical specialty and aberration of our novel imaging system can be analyzed by using the optical design software ZEMAX-EE. The encircled energy diagram of our developed system is shown in Fig. 3, where the horizontal coordinate is the radius, and the vertical coordinate is the normalized fraction of the enclosed energy. The encircled energy diagram is the percentage of total energy enclosed as a function of distance from either the chief ray or the centroid at the image of a point object, while the diffraction-limit curve is for the aberration free encircled energy computed on-axis. In Fig. 3, it can be seen that when using our developed digital imaging system, when an object with a height of 0.5 mm is set at the focal plane of the objective, then the efficiency of collected emission fluorescence from the object is near to the diffraction limit.

The optical path difference (OPD) is a scalar quantity and is identical to the aberration in the tangential direction PX and the sagittal direction PY, respectively. The data plotted in Fig. 4(a) is the optical path difference of our digital imaging system, the vertical axis scale is one wave, and the horizontal scale is the normalized entrance pupil coordinate. The OPD maximum of our digital imaging system is smaller than one wave. The distortion is defined as the real chief ray height, minus the paraxial chief ray height, divided by the paraxial chief ray height, times 100. The distortion values of our digital imaging system are described in Fig. 4(b), where the distortion values in a view field of 0.5 mm are smaller than 0.1
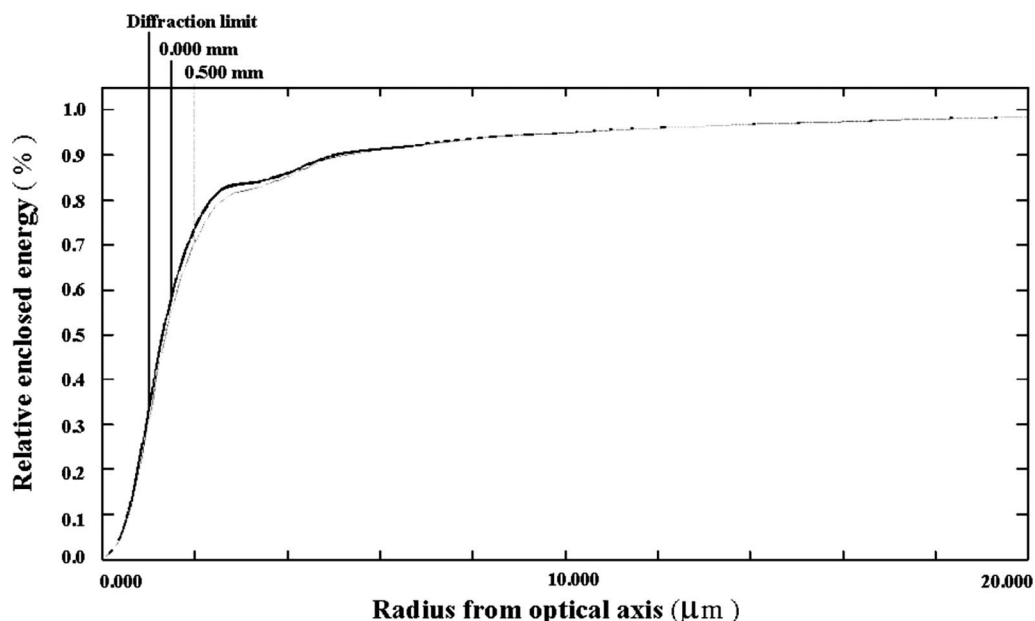
Fig. 3 The encircled energy diagram of the system.

%, and the distortion values to four different wave lengths—530, 570, 620, and 670 nm—are identical. Figure. 4 shows that very little aberration and low distortion limits are hallmarks of our digital imaging system.

2.3 *Constitution of the Digital Imaging Scanning System*

A new *digital imaging scanning system* was built by applying the prior optical design parameters (Fig. 5). A laser with a wavelength of 532 nm was used to irradiate the biochip on the *xy* scanning stage by optical fiber coupled and collimated lenses, and a cut-off was used to control the exposure time and reduce the photobleaching from the laser irradiation. An attenuator was used to adjust the intensity of the irradiating beam to fit with the requirements of different biochip applications. The fluorescence of dye-tagged biological molecules on the biochip was induced and was collected initially by the objective set, then the fluorescence passed through a filter and was imaged on a video CCD (Watec Company Limited,

Japan) by a magnifying lens set. Finally, the fluorescence image of the biological molecule on the biochip is transferred into the computer for digital image processing via an image card.

As illustrated in Fig. 3, this system is an advanced digital imaging scanner for biochip applications characterized by an objective with a high numeral aperture of NA=0.72, a long working distance of 3 mm, and a high efficiency of collecting fluorescence near the diffraction limit. Because an oblique incident laser was used to excite the fluorescence from the biochip, there was very little dark-field irradiation emanating from the background of reflected incident laser light. Generally, an oblique incident beam produces an uneven ellipse spot on the incident plane, shown in Figs. 6(a)–6(c), but the oblique incident beam in our digital imaging scanning system was reshaped into an even round spot on the biochip by a cylinder lens set. The change of the incident spot after reshaping is shown in Figs. 6(d)–6(f). The cylinder lens set was specified as listed Table 2. The power density distribution of
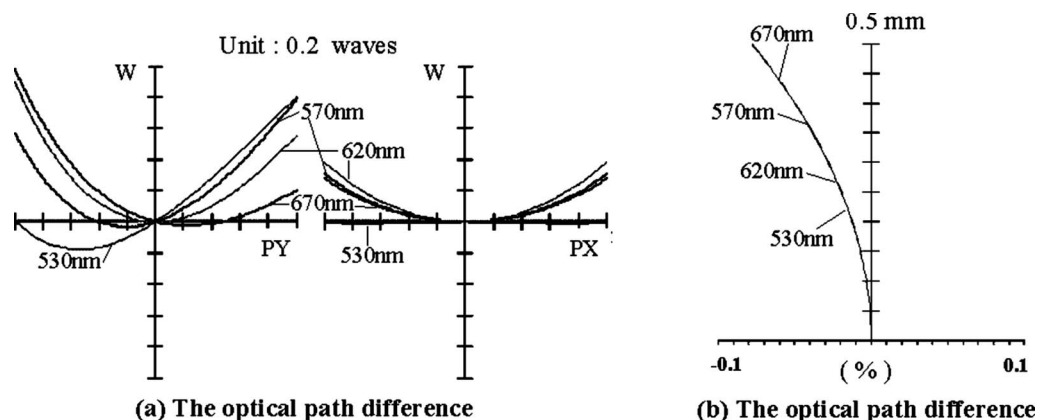
Fig. 4 Optical path difference and distortion of the system.
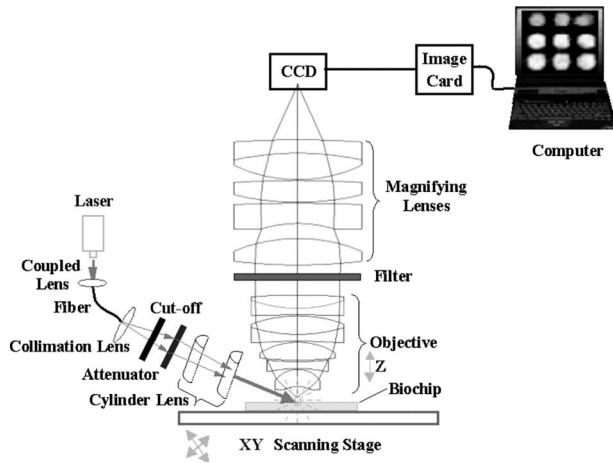
Fig. 5 The developed digital imaging scanning system.

the beam spot before and after reshaping is shown in Figs. 6(c) and 6(f). Because fluorescence intensity is an approximately direct ratio to the power of the exciting beam spot, the even power density distribution of the reshaped beam spot will make a truer fluorescent image of the biochip.

2.4 Restructure Scanning Images

The system has been designed to detect an imaging area of 0.5×0.5 mm with high resolving power in one scan, as shown in Fig. 5. To obtain the large 20×60-mm detection area of a whole biochip, an xy scanning stage is used to move the biochip to obtain a large number of patched images at different positions, and then these patched images are restructured into a large combined image. Generally, large position errors and obviously joined traces tend to occur when a number of high resolution images are patched together. To correct for such join errors, an edge overlap restructuring algorithm was developed and is shown in Eq. (5). Here, $S_1(i,j)$ and $S_2(i,j)$ are two border patched images with a 16-pixel-wide edge overlap area, and M and N are two natural numbers.

Table 2 The mechanism and optical layout of the cylinder lens set (units: mm).

Surface	Radius	Thickness	Glass
1	39.99	2.50	ZK11
2	Infinity	34.91	
3	Infinity	1.50	ZK11
4	15.996		

$$S_{\min} = \min\left\{ \sum_{i=1}^{M} \sum_{j=1}^{N} \left[S_1(i,j) - S_2(i,j) \right] \right\}. \qquad (5)$$

When structuring a combined image from many patched images captured at different scanning positions, the process of restructuring patched images is as follows. First, two border patched images $S_1(i,j)$ and $S_2(i,j)$ were moved to meet the minimum $S_{\min}$ condition, and an optimal matching position for restructuring the patched images was calculated. Second, the patched images $S_1(i,j)$ and $S_2(i,j)$ are cut to remove the eight-pixel-wide edge area from each respective image, and then become two new (nonoverlapping) patched images $S_1'(i,j)$ and $S_2'(i,j)$. Finally, two new patched images $S_1'(i,j)$ and $S_2'(i,j)$ are joined at the optimal matching position. Using this process, image by image, each of the patched images could be restructured into a large combined image. Last, a fine processing and smoothing of the images restores high image quality to the combined image end product. By employing this edge overlap restructuring algorithm for the rapid display of the restructured chip image, the position error can be reduced to 1 pixel, which is about 3 μm in size, and is the minimum chip resolution of our image scanning system. Our system, however, has a $10 \times$ zoom, and when used, the position error of 1 pixel can be reduced to about 0.8 μm. Such high resolution images require significant computing power

(a) The simulating original spot at an incident angle 22°

(b) The real original spot at an incident angle 22°

(c) The power density distribution of real original spot in (b)

(d) The simulating reshaped spot at an incident angle 22°

(e) The real reshaped spot at an incident angle 22°

(f) The power density distribution of real reshaped spot in (e)
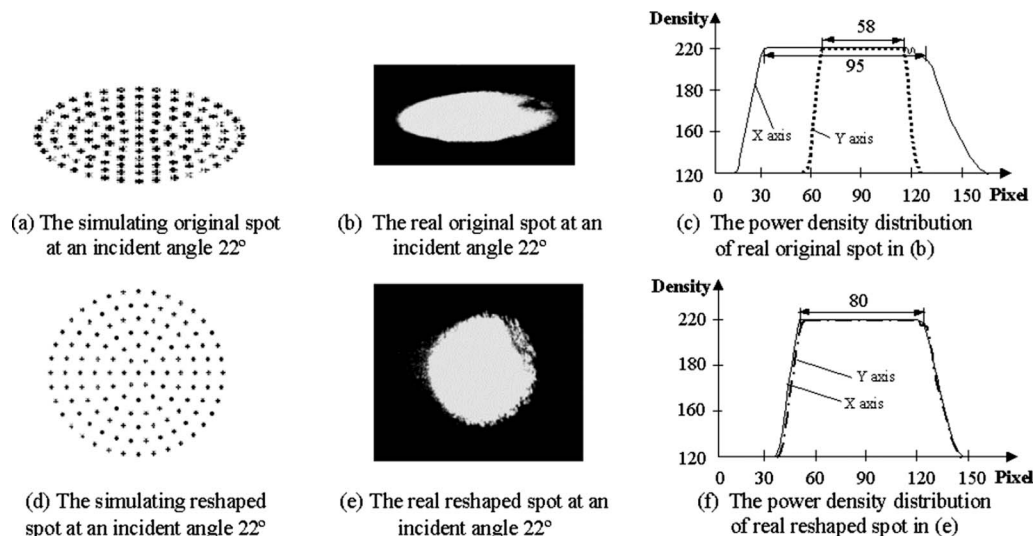
Fig. 6 The reshaping of spots by an oblique incident beam.

(a) The restructured images without the edge overlap algorithm

(b) The restructured images with the edge overlap algorithm
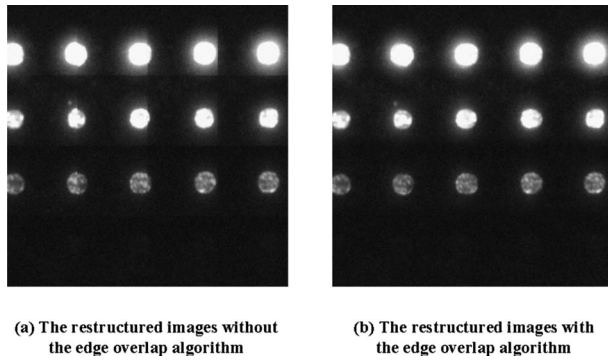
Fig. 7 Comparison of the restructured images.

(a) The original gray images

(b) Binary images with optimum threshold value

Fig. 8 The binary images processed with optimum threshold values.

and storage capacity, and hence the restructured high resolution restructured image is displayed only very slowly. A comparison of restructured images with or without use of the edge overlap algorithm is shown in Fig. 7. A large position error and obviously joined trace can be seen in Fig. 7(a) when the images were restructured without using the edge overlap algorithm. In contrast, Fig. 7(b) shows correction of position error of the patched images and no evidence of joined traces after the edge overlap algorithm was used.

In the last decade, a number of image matching techniques for restructuring have been explored for use during image processing. Examples include area-based matching, which uses windows composed of gray values, and feature-based matching, which uses *a-priori* features extracted in each image.[14–19] There are some disadvantages to using the area-based matching method, including high sensitivity of the gray values to illumination intensity, and the large time taken and large search space needed for matching. There are several different feature-based matching methods, including the gradient across the edge scheme,[15] the correlation scheme,[16,18] and the wavelet scheme.[19] Feature extraction methods are often computationally complex and require both the definition of features and that many parameters are chosen *a-priori*.

To reduce the effect of the gray changes due to illumination intensity and to simplify the definition of the features, we explored the prior edge overlap restructured algorithm. This algorithm only performs a matching feature with minimal gray differences in the edge overlap area over a width of 16 pixels. Except the *a-priori* choice of the 16-pixels-wide edge overlap area from our digital images, there are few other parameters requiring selection. Thus, the absence of complex calculations reduces the time needed for image patching and restructuring. Our developed edge overlap restructured algorithm has proved to be robust for restructuring our scanning patched images and is well suited for high resolution imaging of biochips.

2.5 *Automatic Discrimination of Positive Probes from Scanning Images and Analysis of the Data Matrix of Biochips*

For biochip applications, not only is the scanner required to detect the biochip and obtain an image, but data need to be extracted from the scanning images for analysis of information based on the character of the signal spots of the probes arrayed on the biochip. An automatic algorithm was developed capable of discriminating positive probes, extracting information from the biochip images and for producing a data matrix analysis of all probes on the biochip. The algorithm can perform the tasks automatically by the following steps.
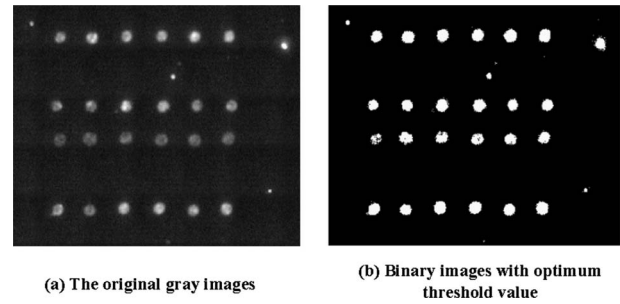
Step 1. Choose an optimum threshold value for the binary processing of images by use of the Otsu algorithm.[12] First, the gray-level histogram of digital images is defined as $PHS(s)$, where s is the gray level of pixels in digital images. The gray class average $\mu(K)$ and the gray class histogram $\omega(K)$ are defined respectively as,

$$\mu(k) = \sum_{s=1}^{k} (s-1) PHS(s), \tag{6}$$

$$\omega(k) = \sum_{s=1}^{k} PHS(s), \tag{7}$$

where k is a natural number.

A class analyzing function is described as,

$$\sigma_B(k) = \frac{[\mu(k)\omega(k) - \mu(k)]^2}{\omega(k)[1 - \omega(k)]}. \tag{8}$$

When the class analyzing function $\sigma_B(k)$ is maximum, an optimum threshold value T for the binary images is obtained as $T = k - 1$. The binary processing of images is shown in Fig. 8, where Fig. 8(a) is the original gray image, and Fig. 8(b) is the binary image with an optimum threshold value.

Step 2. Calculate the center and the space of the columns and rows of the microarray probes on the biochip from the binary images.

If the binary images are described as a data matrix $S_{(m,n)}$, then the center of the columns and rows of microarray probes can be positioned at the maximum of the gray sum of pixels along the horizontal direction and along the vertical direction as shown in Figs. 9(a) and 9(b), where n and m are two natural numbers.

The sum of gray of all pixels in the vertical direction is

$$\text{row}(\chi) = \sum_{y=1}^{n} S(x,y), \quad y = 1, 2, \ldots, n. \tag{9}$$

The sum of gray of all pixels in the horizontal direction is

The gray sum of all pixels at horizontal direction

(a)

The gray sum of all pixels at vertical direction

(b)
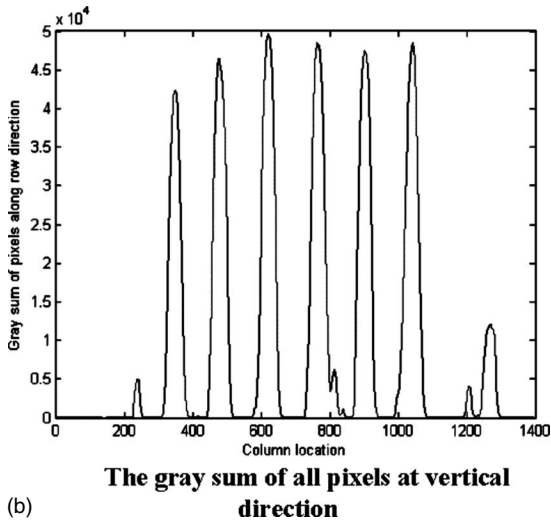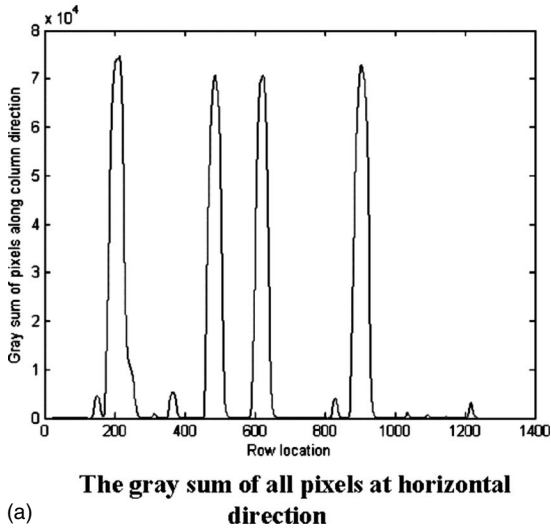
Fig. 9 The gray sum of pixels along the horizontal and vertical directions.

$$\mathrm{col}(y) = \sum_{x=1}^{m} S(x,y), \quad \chi = 1,2,\ldots,m. \quad (10)$$

The space of the row probes can be calculated by using the maximum intensity spectrum of the Fourier transform of row(x) in the vertical direction, and the space of column probes can also be calculated by using the maximum intensity spectrum of the Fourier transform of col(y) in the horizontal direction.

The Fourier transform of the gray sum of pixels along the vertical direction is

$$F\{\mathrm{row}(x)\} = F_{\mathrm{row}}(p),$$

$$= \sum_{x=1}^{m} \mathrm{row}(x)\exp[-j2\pi(p-1)(\chi-1)/n],$$

where $x = 1,2,\ldots,m.$ \quad (11)

(a)

(b)
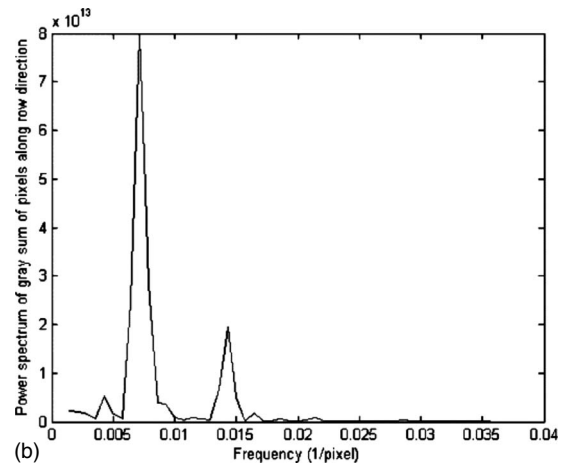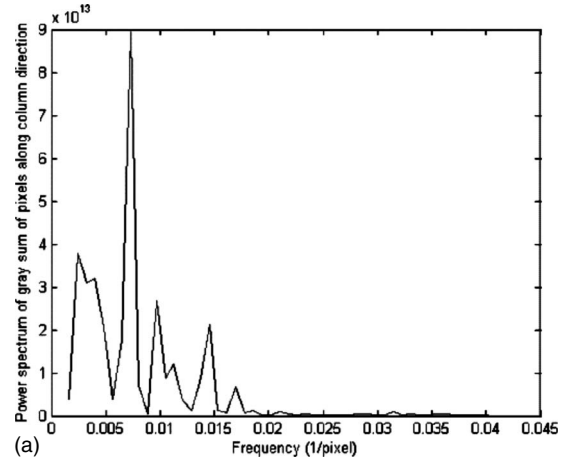
Fig. 10 Fourier transfer of the gray sum of images.

The Fourier transform of the gray sum of pixels along the horizontal direction is

$$F\{\mathrm{col}(y)\} = F_{\mathrm{col}}(q) = \sum_{y=1}^{n} \mathrm{col}(y)\exp[-j2\pi(q-1)$$

$$\times(y-1)/m], \quad \text{where } y = 1,2,\ldots,n. \quad (12)$$

The intensity spectrum of the Fourier transform along the vertical direction is $|F_{\mathrm{row}}(p)|^2$, and the intensity spectrum of the Fourier transform along the horizontal direction is $|F_{\mathrm{col}}(q)|^2$, which are shown in Fig. 10.

The frequency $f_{i\mathrm{max}}$ is obtained at the maximum intensity spectrum of the Fourier transform along the vertical direction. The frequency $f_{j\mathrm{max}}$ is obtained at the maximum intensity spectrum of the Fourier transform along the horizontal direction.

The space d_i of the row probes is calculated as $d_i = 1/f_{i\mathrm{max}}$.

The space d_j of the column probes is calculated as $d_j = 1/f_{j\mathrm{max}}$.

Step 3. Discriminate the signal spots of the microarray probes and produce their data matrix.

(a) The grid intersected images   (b) The aims discriminating marks   (c) The end processed pseudocolor images
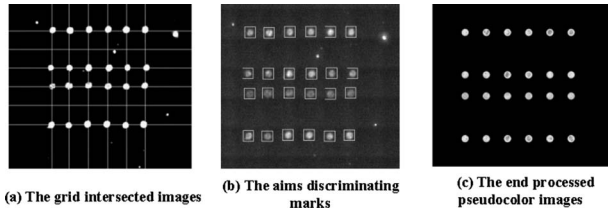
Fig. 11 Automatic target discrimination and pseudocolor processing.

After this step, the center and the space of signal spots of the microarray probes from step 2 are considered, and the following process is then used to remove the noise and retain the effective spot signals for the calculation of the signal intensity of probes.

A normal circle disperse $ND(r_0)$ is defined as,

$$ND(r_0) = \int 2\pi r^2 dr/(\pi r_0^2), \tag{13}$$

where r_0 is the radius of the probes, and generally

$$r_0 \leq \frac{1}{8}\sqrt{d_i^2 + d_j^2},$$

where d_i is the space of the row probes, and d_j is the space of the column probes.

An actual signal spot disperse $AD(L)$ is defined as:

$$AD(L) = \frac{\sum_{i=1}^{l1}\sum_{j=1}^{l2}(i^2 + j^2)^{1/2}}{l1 \times l2}, \tag{14}$$

where l_1 and l_2 are two natural numbers,

$$L = \frac{1}{2}\sqrt{l_1^2 + l_2^2}.$$

When $i=1$ to l_1 and $j=1$ to l_2, $(l_1^2+l_2^2)/4=r_0^2$, then the signal intensity of spots is $S_{(i,j)} > 0$.

The ratio of the disperse RD_{NA} is calculated as:

$$RD_{NA} = AD(L)/ND(r_0). \tag{15}$$

In an ideal circular probe signal spot, $RD_{NA}=1$. Typically, however, an actual signal spot image of biochip probes is an irregular circular spot, then $RD_{NA} \leq 1$. In our actual scanning images of biochip probes, an experimental ratio of the disperse RD_{NA} was summarized as $0.5 \leq RD_{NA} \leq 1$, allowing the noise to be removed and the effective signals of the discriminated probe spots retained.

The center position and space of the retained effective signal spots can be calculated by using the center and the space of signal spots of microarray probes obtained in step 2. A grid of intersecting images can be obtained, as shown in Fig. 11(a), and the effective signal spots of the biochip images are indicated in Fig. 11(b). Image processing was then undertaken to remove the noise and keep the effective signal spots for the pseudocolor images shown in Fig. 11(c). The average (or medium) signal intensity of these effective probes was calculated from the original scanning images of biochips with a radius r_0. A signal data matrix of probes as shown in Table. 3 was

Table 3 The analysis data matrix.

Row	Column					
	1	2	3	4	5	6
1	141.04	179.19	160.28	157.85	183.01	171.74
2	0.00	0.00	0.00	0.00	0.00	0.00
3	125.63	133.38	178.93	166.23	130.40	141.10
4	98.20	112.60	118.52	114.04	117.84	117.20
5	0.00	0.00	0.00	0.00	0.00	0.00
6	149.87	125.37	174.10	174.06	153.19	176.15

obtained, which can be used to analyze and determine the positive or negative probes of biochips by an experimental threshold.

Employing the previously developed algorithms for automatic discriminating of targets, all effective probes can be discriminated from the reconstructed and combined scanning images of the biochips. Thus, an experimental analysis data matrix from the DNA microarray or protein microarray can be obtained.

2.6 Detection Sensitivity and Resolving Power of the System

The detection sensitivity of the newly developed digital imaging scanner was tested as shown in Fig. 12(a), where a Full-Moon normal molecular density validated-biochip (Full Moon BioSystems, Sunnyvale, California) was used. The unit of density is the molecule number per square micron, and the

Images								
	1	2	3	4	5	6	7	8
Density	0.561	1.12	2.24	4.49	8.97	17.9	35.9	71.8
Signal	45.39	46.90	49.41	54.58	69.11	89.31	135.59	206.98

(a)   Scanning a checked biochip of Full Moon

(b)
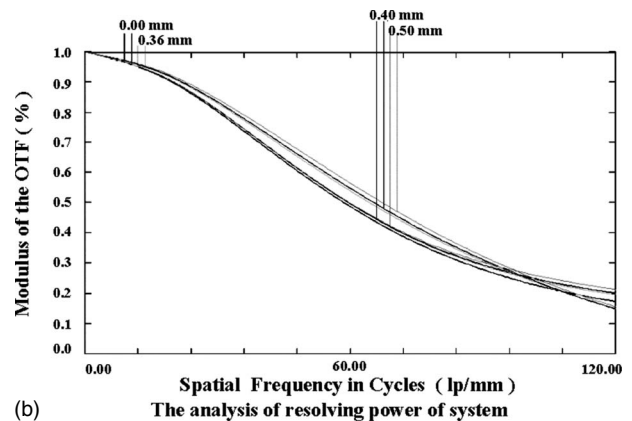
Fig. 12 The sensitivity and resolving power of the developed digital imaging scanner.
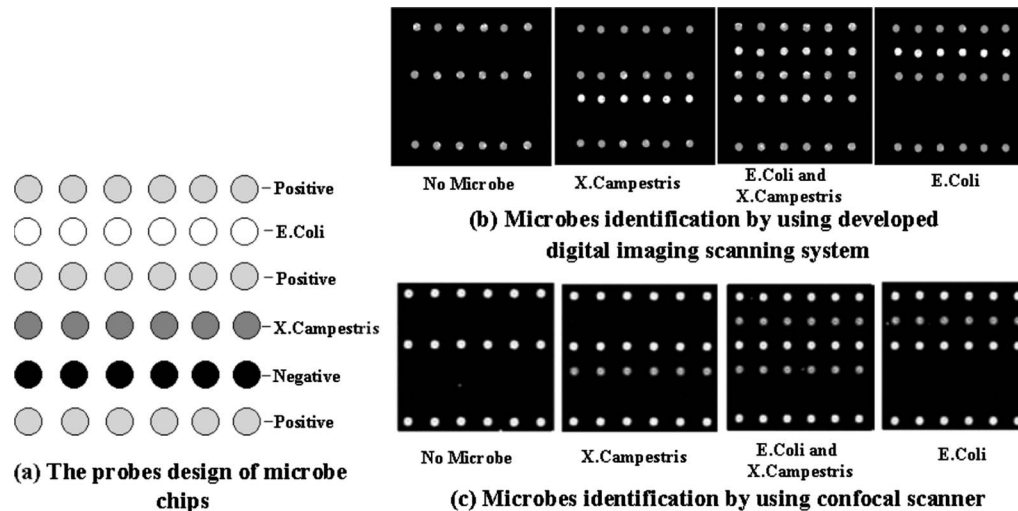
Fig. 13 Identification of *E. coli* and *X. campestris.*

signal is a relative intensity within the range of 0 to 250. In Fig. 12(a), the molecule with density 0.561 fluors/μm^2 was detected with a signal of 45.39 where the signal-to-noise ratio SNR was larger than 2. Figure 12(b) shows the analysis of the spatial frequency of the system on the imaging plane, with more than 120 lines/mm. Because the system has a zoom of 2.26, the object resolving power is then larger than 300 lines/mm, which indicates that our developed digital imaging scanner has a high resolving power of about 3 μm.

3 Biomedical Application of Biochips

Examples of two biomedical applications of biochips were performed using the developed digital imaging scanning system. These were the identification of bacteria using gene chips and the detection of serum antibodies using protein chips.

3.1 Identification of Bacteria by Gene Chips

The identification of bacteria using gene chips is an important parallel method capable of simultaneously detecting numerous different bacterial species in a single diagnostic test.

The surface of the glass chip was modified for covalent bonding to specific gene probes, and the chip was printed with four 6×6 probe arrays by using the SmartArrayer™-48 (CapitalBio, Beijing, China), as shown in Fig. 13(a). The array comprises one row of *Escherichia coli* probes for the chaperone Hsp70 gene, one row of the *Xanthomonas campestris* probes for the HtpG gene, one row of negative probes as quality report marks of the chip hybridization and three rows of positive probes used to demonstrate successful amplification. Normally, for the validation of results on the chip, the negative probes show a blank (or zero) signal, and the positive probes report a high fluorescent intensity signal. Conversely, if the negative probes are not blank (or have a high signal), or the positive probes report a low (or blank) signal, these indicate that either the chip is defective or that the experimental protocols have failed, and thus the experimental results will not be valid.

The repetition of the same six probes in a row demonstrates the chip credibility and generates independent repeated

signals for statistical analysis of the experiment. If *E. coli* were present in a sample, then the row of *E. coli* probes will show a high signal. Similarly, if there were *X. campestris* in a sample, the row of *X. campestris* probes will show a high signal, and if there are neither bacteria present, then their reporter probes will show a low (or zero) signal. The bacterial genes present in a sample are first amplified by PCR to produce fluorescently labeled DNA fragments that are complementary to the chip bound probes, and which can be selectively hybridized to them. As shown in Fig. 13, fluorescence signals detected by our developed digital imaging scanning system were compared to the signals detected by another commercial confocal scanner (Scanner Array 4000B). Figure 13(b) shows the detection results by using our developed digital imaging scanning system, and Fig. 13(c) are the results obtained using the Scanner Array 4000B confocal scanner. Both scanning images show the same identification results, with good specific and parallel outcomes. However, the different color processing of the scanning diagrams illustrates differences between our digital imaging scanning system and the Scanner Array 4000B confocal scanner, with our system generating higher quality images.

3.2 Detection of Serum Antibodies by Protein Chips

The developed digital imaging scanning system is also useful for fluorescence detection of the immuno-reactions of proteins on chips. We describe here a protein microarray chip (surface modified with a gel for the covalent attachment of the antigen spots) for the parallel detection of autoantibodies in the serum of patients with several different autoimmune diseases. These include systemic supus erythmatosis (SLE), mixed connective tissue disease (MCTD), Sjögren's syndrome (SS), systemic sclerosis (SSc), dermotomyositis (DM), and polymyositis (PM). The protein microarray chip was printed in a 7×6 array of antigen probes using the CapitalBio SmartArrayer™-48 and the noncontact spray head. The array, as shown in Fig. 14(a), includes two systemic quality controls (QC), a blank control (BC), a Sjögren's syndrome B antigen (SSB), a reaction control (RC), a sclerosis 70 kDa (Scl) anti-

(a) Probes design

(b) The image by using developed digital imaging scanning system

(c) The image by using commercial confocal scanner
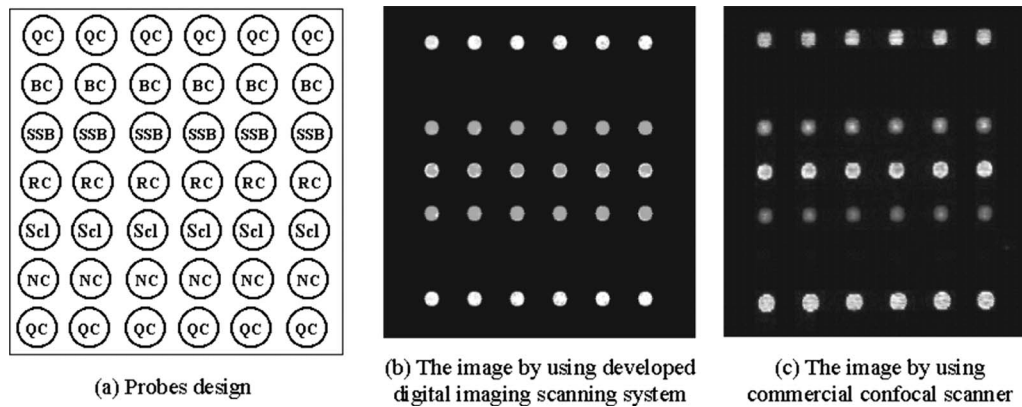
Fig. 14 Detection of patient serum autoantibodies by a protein chip.

gen probe, and a negative control (NC). Purified autoantigens (SSB, Scl) were also immobilized on the chip. The protein microarray chip was incubated with 30 μL of a mixture of the serum (diluted 1:100 with PBST) from two patients with different diseases (anti-SSB and anti-Scl), for 30 min at room temperature. After being rinsed and washed one time for 5 min with PBST, the chip was incubated with 30 μL of Cy3-labeled goat antihuman IgG antibody for 30 min at room temperature. After another rinse and several washes with PBST for 5 min, the chip was briefly centrifuged to dry it. The protein microarray chip was then scanned using our developed digital imaging scanning system in Fig. 14(b), and the Scanner Array 4000B confocal scanner in Fig. 14(c). The results of scanning images clearly showed that this mixed sera contained both anti-SSB and anti-Scl autoantibodies. Both systems gave the same autoantibody detection results; however, the differences in color processing of the scanning images by our developed digital imaging scanning system and the commercial confocal scanner are apparent, with our system generating higher quality images.

4 Discussion and Conclusion

The newly developed digital imaging scanning system was shown to perform well with two biomedical biochip applications for the detection of fluoro-tag DNA hybrids and for the detection of fluoro-tagged immuno-reacted proteins. Comparing our system to a commercial confocal scanner showed that both reliably produced the same detection results; however, our image analysis software generated superior end images. The long working distance of the newly developed digital imaging scanner has particular advantages for working with biochips enclosed within a hybridization gasket, or for conventional microscope slides with thick cover slips, or even with a thick layer of culture liquid. The scanner has a high scanning resolving power of 3 μm and a sensitivity of detected fluorescence of 0.5 fluors/μm^2. The specially developed edge overlap restructuring algorithm and the developed target discriminating algorithm are each also very important elements of the system, and are necessary for obtaining excellent images of large objects with quite clear definition, high contrast, and a high signal-to-noise ratio. The developed data analysis matrix is another important element needed to determine the positive and negative probe signals on the biochips.

When compared to other common microscope objective designs where the objective of a typical microscope has a numerical aperture of NA=0.65 and a working distance smaller than 1 mm (such as the Zeiss plan objective 440050, NA=0.65, w_d=0.6 mm, and the Nikon CFI plan objective model, NA=0.65, w_d=0.57 mm), it is obvious that the optical design of the newly developed digital imaging scanning system is highly advanced, with an optimum combination of lenses, including a high numerical aperture of 0.72, and a long working distance of 3.0 mm. The use of only seven lenses and only three different kinds of optical glass of ZK7, ZK11, and ZF2 are also beneficial. The limited number of glasses and lenses reduces the compound aberration and error inherent in the use of large numbers of lenses and multiple glasses. In addition, these glass materials favor manufacture with small material error and small machining error.

Biochips have different reaction environments to the common *in solution* DNA hybridization and protein immunoreactions. Biochips allow multiple highly specific reactions to be assayed in parallel and require only nanoliter volumes of sample. As demonstrated, with identification of species-specific bacterial genes and human serum autoantibodies without cross talk, biochips can be applied for the detection of numerous different types of genes or autoantibodies. Currently, several tens of thousands of genes (or proteins) can readily be printed on a 20×60-mm glass biochip, and several tens of thousands of genes (or proteins) can be simultaneously identified in parallel in a single test by using our developed digital imaging scanning system.

References

1. S. P. Fodor, J. L. Read, M. C. Pirrung et al., "Light-directed, spatially addressable parallel chemical synthesis," *Science* **251**(4995), 767–773 (1991).

2. P. O. Brown and D. Botstein, "Exploring the new world of genome with DNA microarrays," *Nat. Genet.* **21**(suppl.1), 33–37 (1999).

3. Y. Guo, H. Y. Guo, L. Zhang et al., "Genomic analysis of anti-HBV activity by siRNA and lamivudine in stable HBV-producing cell," *J. Virol.* **79**, 14392–14403 (2005).

4. G. MacBeath and S. L. Schreiber, "Printing proteins as microarrays for high-throughput function determination," *Science* **189**, 1760–1763 (2000).

5. J. Kononen, L. Bubendorf, A. Kallioniemi et al., "Tissue microarrays for high-throughput molecular profiling of tumor specimens," *Nat. Med.* **4**(7), 844–47 (1998).

6. Y. Huang, S. Joo, M. Duhon et al., "Dielectrophoretic cell separation and gene expression profiling on microelectronic chip arrays," *Anal. Chem.* **74**, 3362–3371 (2002).

7. L. Smith and A. Greenfield, "DNA microarrays and development," *Hum. Mol. Genet.* **12**, R1–R8 (2003).

8. T. R. Golub, D. K. Slonim, P. Tamayo et al., "Molecular classification of cancer: class discovery and class prediction by gene expression monitoring," *Science* **286**, 531–537 (1999).

9. C. Debouck and P. N. Goodfellow, "DNA microarrays in drug discovery and development," *Nat. Genet.* **21**, 48–50 (1999).

10. W. Luigi, B. David, and L. Irving, "Transcription factor profiling in individual hematopoietic progenitors by digital RT-PCR," *IEEE Trans. Pattern Anal. Mach. Intell.* **103**(47), 17807–17812 (2006).

11. R. Daniel, S. Yoko, X. Ioannis et al., "Microarray deacetylation maps determine genome wide functions for yeast histone deacetylases," *Cell* **109**, 437–446 (2002).

12. G. Y. Wang, Y. L. Zou, and Y. Ling, "An algorithm for salience based local recursive OTSU segmentation," *J. Huazhong Univ. Sci. Technol.* **30**(9), 57–59 (2002).

13. S. Nagl, M. Schaeferling, and O. S. Wolfbeis, "Fluorescence analysis in microarray technology," *Microchimica Acta* **151**(1–2), 1–21 (2005).

14. C. Heipke, "Overview of image matching techniques," *Frankfürt: OEEPE Official Publications*, pp. 173–189 (1996).

15. W.-H. Liao, C.-L. Yu, M. Bergsneider et al., "A new framework of quantifying differences between images by matching gradient fields and its application to image blending," *Nuclear Sci. Symp. Conf. Record IEEE* **2**, 1092–1096 (2002).

16. A. J. Fitch, A. Kadyrov, W. J. Christmas et al., "Fast robust correlation," *IEEE Trans. Image Process.* **14**(8), 1063–1073 (2005).

17. F. Zhao, Q. Huang, and W. Gao, "Image matching by normalized cross-correlation," *2006 IEEE Intl. Conf.* **2**, 729–732 (2006).

18. A. F. Elaksher, "Refinement of correlation-based DEM using linear features," *J. Eng. Appl. Sci.* **54**(2), 155–170 (2007).

19. X. R. Dai and L. Y. Chen, "A wavelet-based image matching scheme," *Proc. SPIE*, 5985, 658–663 (2005).